Laser additive manufacturing and post-heat treatment on microstructure and mechanical properties of 9Cr steel

Junyi Feng[a,b], Peilei Zhang[a,b,c,*], Zhiyuan Jia[a,b], Zhishui Yu[a,b,*], Chao Fang[d,*], Hua Yan[a,b], Haichuan Shi[a,b], Yingtao Tian[e], Fan Xie[f]

[a]School of Materials Engineering, Shanghai University of Engineering Science, Shanghai 201620, China

[b]Shanghai Collaborative Innovation Center of Laser of Manufacturing Technology, Shanghai 201620, China

[c]Fraunhofer Institute for Laser Technology ILT, Aachen 52074, Germany

[d]Institute of Plasma Physics, Chinese Academy of Sciences, Hefei 230031, China

[e]Department of Engineering, Lancaster University, Lancaster LA1 4YW, United Kingdom

[f]Huarui(jiangsu) Gas turbine services limited company, Nantong, 226000, China

ABSTRACT

9Cr steel is a material that has been widely used in pressure vessel parts in thermal power plants and nuclear power plants, and has good high-temperature creep properties. Laser Melting Deposition (LMD) is a promising method for preparing complex 9Cr steel components. It provides a rare opportunity to improve existing designs and produce fine features and complex geometries with higher efficiency. The LMD-9Cr steel sample has high density, the maximum tensile strength of the sample is 1057.75MPa, which is much higher than the standard cast 9Cr steel of 650MPa. We use 760°C tempering heat treatment, after heat treatment, the average grain size of the material is reduced, the Charpy impact performance is improved, and the tensile strength and microhardness are slightly reduced. Although the tempering heat treatment greatly reduces the average grain size of the sample by 35.59%, but at the same time the tempering heat treatment greatly reduces the high dislocation density of lath martensite, and the supersaturation behavior of Cr, W and C elements weakens the effect of solid solution strengthening. In addition, through the nanoindentation test, we found that although the $M_{23}C_6$ precipitated phase can harden the material, at the micro level, the elastic modulus and nano-hardness of the precipitated phase are lower than that of the homogeneous phase.

Keywords: Laser Melting Deposition (LMD); 9Cr steel; Different powder size; Post-heat treatment; Mechanical properties; Microstructure

Introduction

With the rapid development of society and economy, electricity consumption and environmental pollution are

* Corresponding authors: Peilei Zhang (peilei@sues.edu.cn) , Zhishui Yu (yu_zhishui@163.com) and Chao Fang (fangchao@ipp.ac.cn)

exploding worldwide. Nuclear fusion power generation has attracted widespread attention because of its abundant fuel resources, zero carbon emissions and low operating costs. 9Cr high-strength steel, also known as 9Cr-1Mo steel or P91 grade steel, this steel exhibits good high temperature performance by virtue of its low activity, excellent thermal conductivity and superior radiation resistance, high stress corrosion cracking capability and expansion resistance to neutron radiation environments. 9Cr high-strength steel is one of the best candidates as a structural material for modern ultra-supercritical (USC) power plants, with high creep resistance, suitable for higher temperature (>650°C) operating environment[1–5].

9Cr steel is typically joined using welding processes such as friction stir welding (FSW), submerged arc welding (SAW), gas tungsten arc welding (GTAW) and gas metal arc welding (GMAW)[6–8]. However, no matter which welding method is used, there is an unavoidable problem when welding 9Cr steel, which is that the strength of the welded joint, especially the heat affected zone (HAZ), differs from that of the base material, thus affecting the performance of the whole part. In recent years, with the high demand for accuracy and efficiency, additive manufacturing (AM) is a promising method for fabricate 9Cr steel. It has the advantages of high efficiency, high precision, and can be formed in a single process. The methods commonly used for additive manufacturing include wire arc additive manufacturing (WAAM), electron beam melting (EBM) and laser engineered net forming (LENS). LENS can be divided into two categories according to the powder delivery method, one is laser melting deposition (LMD) based on simultaneous powder delivery, which is mainly used for rapid forming of large and complex parts, but the part dimensional accuracy is not high and post-processing is required to meet the application specifications; the other is selective laser melting (SLM) technology based on powder bed system with high forming accuracy but limited processing part size[9–11], which is mainly used for direct precision forming of small and medium-sized complex parts.

The organization and properties of metallic materials are greatly influenced by the fabrication method, and the organization state before heat treatment also has a great influence on the mechanical properties. 9Cr steel fabricated by laser additive technology has a deposition state organization characterized by epitaxial growth of dendrites along the deposition heightening direction.

After the additive manufacturing, a post heat treatment process is required to improve the overall properties of the manufactured part. The purpose of releasing residual stresses and improving mechanical properties is achieved by heat treatment[12,13]. The most common heat treatment recommended by researchers is a heat treatment at 1050°C for 40 minutes (normalized heat treatment) + 760°C/2 hours (tempering heat treatment) to obtain carbide precipitates[14]. The normalizing heat treatment at 1050°C can eliminate the heterogeneity of microstructure to

some extent. At this normalizing temperature, the precipitated phase will partially melt, while the unmelted precipitated phase will exhibit coarsening properties during the heat treatment[15,16]. The tempering heat treatment temperature is controlled at 760°C, because the α-phase recrystallizes when the heating temperature reaches 760°C (the recrystallization temperature of 9Cr steel), the slat grains gradually transform into equiaxed crystals, and the dislocation density decreases[17]. The post-weld normalizing and tempering (PWNT) heat treatments lead to a certain degree of element homogenization and disappearance of the dendritic structure, achieving an optimal combination of strength and ductility[18,19].

In this study, we fabricated different sizes of 9Cr steel using laser coaxial powder feeding technique and designed a new post heat treatment process for additively manufactured materials instead of the traditional heat treatment of wrought materials guided by thermodynamic modeling to optimize the mechanical properties of LMD-9Cr steel. The effects of different powder particle size preparation and post heat treatment on microstructure and mechanical properties were investigated using optical microscopy (OM) and scanning electron microscopy (SEM) combined with X-ray diffraction (XRD) and electron backscatter diffraction (EBSD) techniques and nanoindentation to analyze the effects of the LMD-9Cr steel processes and the variation mechanism of its heat treatment.

2. Experimental procedures

2.1 Materials

The material used in this study is 9Cr steel powder prepared by the method of atomization comminuting process. The chemical composition of 9Cr steel powder is shown in Table 1. Different particle sizes (<25 μm, 15~53 μm, 45~105 μm, >100 μm) 9Cr steel powder is used for laser melting deposition. In order to manufacture 9Cr steel with good properties, powders with excellent fluidity are required. The microscopic morphology of the powder is shown in Figure. 1. The powder has good sphericity and a large number of planetary powders can be seen in the powder used in Figure. 1. This form of powder has a high packing density, and the small voids in the large particles are filled by the small particles, and the fluidity and stacking density are optimized, which is very suitable for additive manufacturing.

Table 1. Chemical composition of powders(wt%).

Element	Fe	Cr	Ta	V	W	Si	Mn	Nb	C
Content	Bal.	8.90	0.14	0.20	1.43	0.05	0.49	0.07	0.09

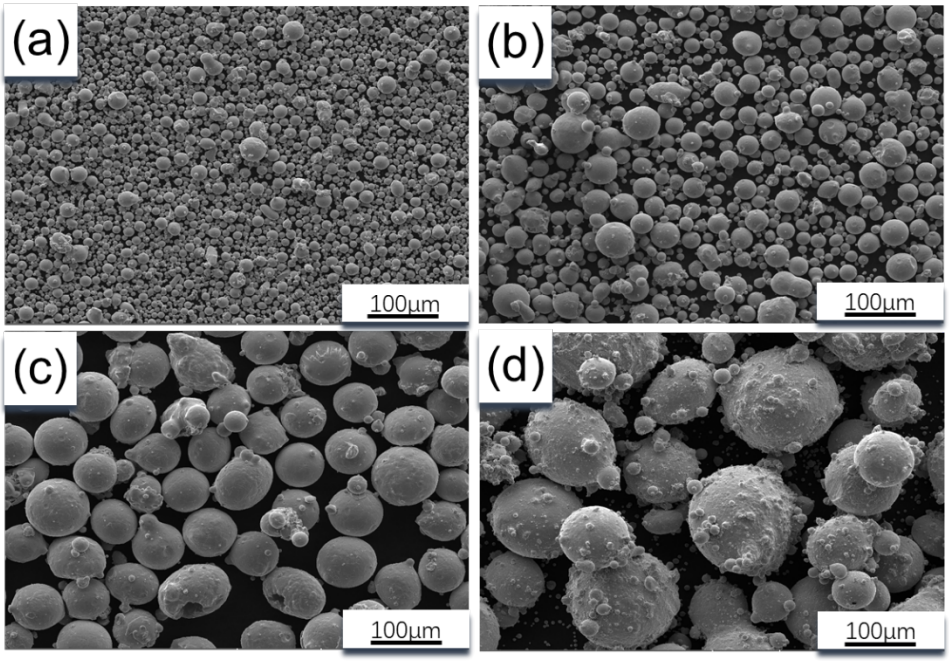

Figure. 1. SEM characterization of powder morphology, (a) <25 μm, (b) 15~53 μm, (c) 45~105 μm, (d) >100 μm.

2.2 LMD process parameters and post heat treatment

Coaxial powder feeding technology was applied in this study, we used IPG YLS-5000 fiber laser and ABB robot linkage system for additive manufacturing of 9Cr steel, the used coaxial powder feeding system is shown in Figure. 2. The schematic diagram of the laser coaxial powder feeding technique for manufacturing samples is shown in Figure. 2(b), the laser head is mounted on the six-axis ABB robot to control its motion trajectory. The specific process parameters used include: laser scanning speed of 10 mm/s, laser power of 2700 W, scanning pitch of 2.4 mm; relevant parameters of the powder feeder include powder feeding speed of 5 rad/min, powder carrier flow rate of 20 L/min, protective gas (Ar) flow rate of 40 L/min, and the manufactured sample size of 140*40*15 mm^3.

In order to eliminate the anisotropy of the as-built microstructure and obtain uniform performance in the 9Cr steel structure, it is necessary to homogenize the as-built matrix. The heat treatment process is set according to the recrystallization temperature (760°C) of 9Cr steel, and a vacuum furnace is used for heat treatment. The ultimate vacuum is 6.7×10^{-4}, heated at 760°C for 2h and then cooled in the furnace, which is equivalent to high temperature tempering heat treatment process.

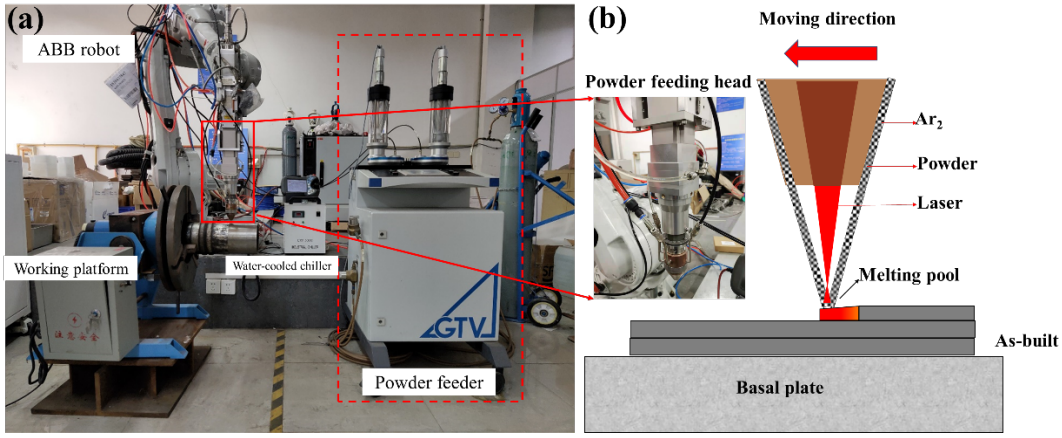

Figure. 2. Coaxial feeding system, including ABB robot and feeding machine: (a) Operation system, (b) Schematic diagram of laser coaxial powder feeding system.

2.3 Thermodynamic modeling

Thermodynamic calculations for 9Cr steel were simulated using Thermo-Calc thermodynamic software. Based on the chemical composition of the powder, a phase fraction-temperature relationship was predicted, as shown in Figure. 3(a). The equilibrium model predicts that the MX phase, i.e., (Nb, V) (C, N), forms at temperatures below 1450 K and remains in the matrix at room temperature. The $M_{23}C_6$ precipitated phase forms below 1100 K and the Laves_C14 phase begins to form at temperatures below 650 K. Scheil-Gulliver solidification simulations are shown in Figure. 3(b) and can broadly predict the nonequilibrium phases in as-built samples. The δ-ferrite and austenite are predicted to be the dominant phases, but during actual cooling, austenite is further transferred to martensite in the 9Cr steel.

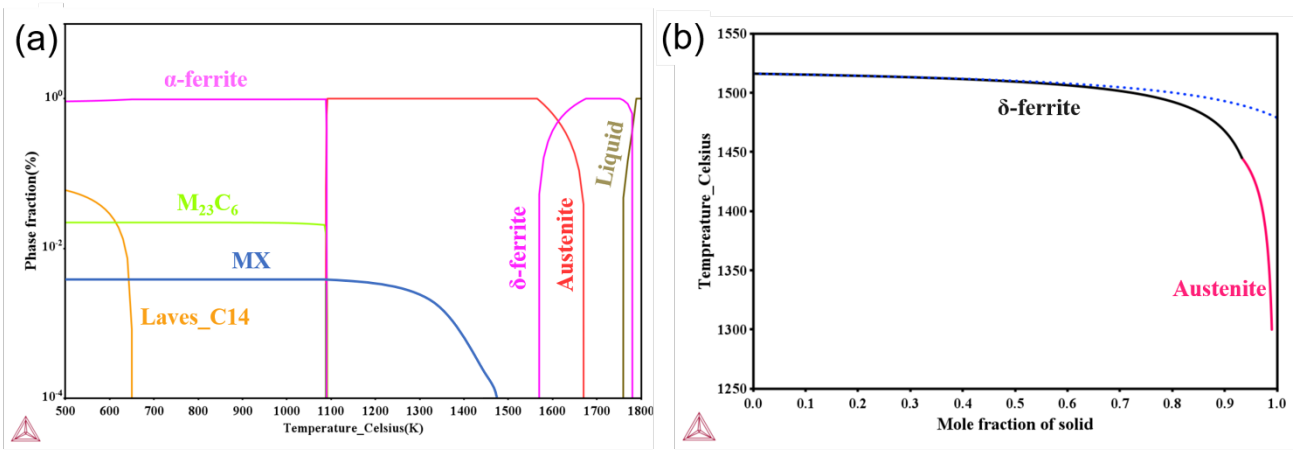

Figure. 3. (a) Thermodynamic prediction for 9Cr steel using Thermo-Calc software (phase fraction – temperature, (b) nonequilibrium simulation using the Scheil–Gulliver model.

2.4 Metallographic characterization and Mechanical testing

Additively fabricated samples were cut from the substrate using wire cutting, metallographic specimens were cut from different powder constructed samples, heat treated, they were mechanically polished and then the samples were etched using Keller's reagent and the microstructures of the as-built and heat-treated samples were studied using optical microscope (OM) and scanning electron microscope (SEM). To further understand the grain and phase composition of the sample, electron back-scattered diffraction (EBSD) and X-ray diffraction (XRD) techniques were used to analyze the sample.

Sample microhardness was measured using a Vickers microhardness tester (HX-1000TM/LCD) at a load of 300g for both vertical and parallel scan paths with a hold load time of 10s. The standards of impact samples and tensile samples used in this experiment are shown in Figure. 4. Tensile samples are made according to the standard ASTM-E8-16a, and Charpy impact test samples are made according to GB/T229-2007. The tensile strength was tested on a CMT5150 universal tester using a tensile speed of 1 mm/min. The impact test equipment was a drop hammer impact tester, tester model INSTRON9350. Figure. 5 shows the tensile and Charpy impact specimens prepared in this experiment.

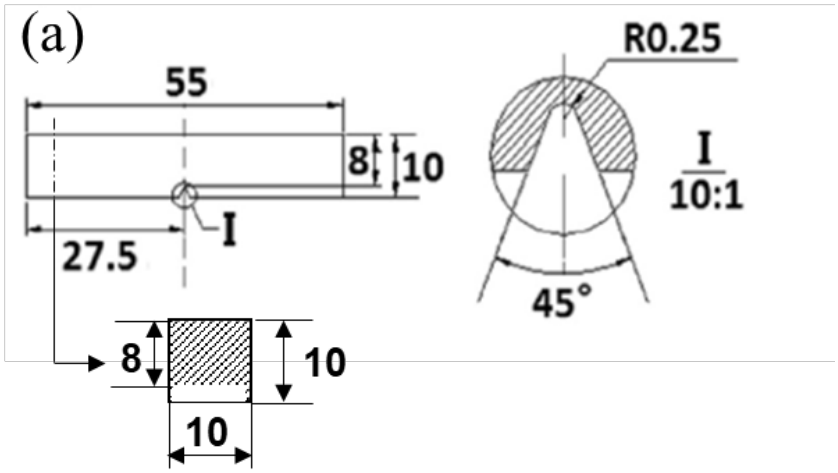

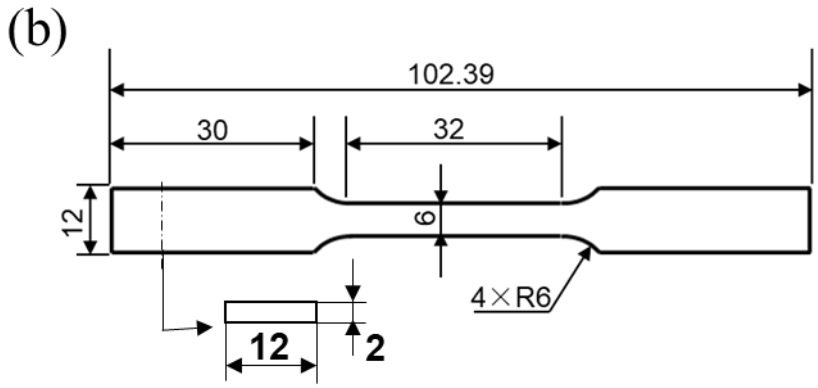

Figure. 4 (a) Standard for Charpy impact specimens (GB/T229-2007) , (b) Standard for tensile specimens (ASTM-E8-16a) .

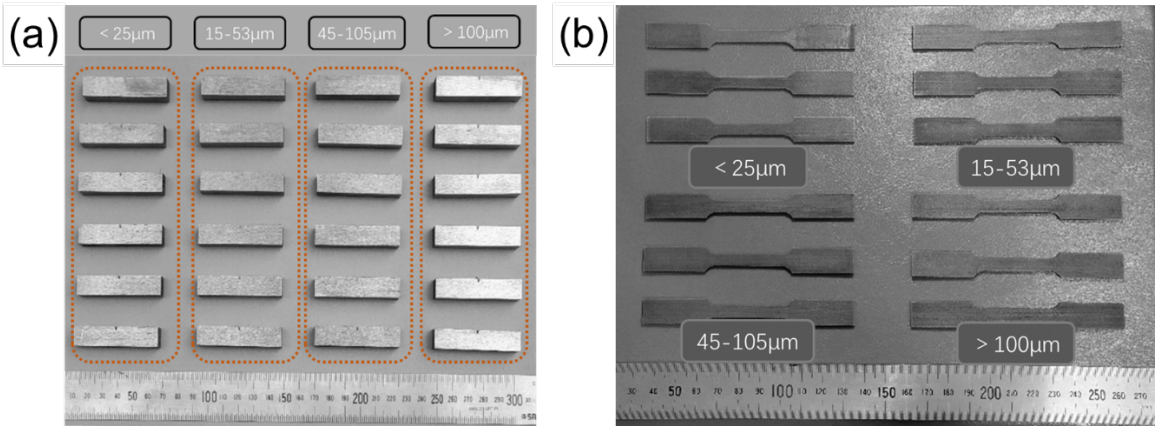

Figure.5 (a) Charpy impact test sample (b) Tensile test sample.

3. Results and discussion

3.1 Microstructural Characterization

After corrosion, it can be clearly seen from Figure. 6(a) that along the construction direction, the as-cast 9Cr steel has obvious stratification phenomenon. Due to the multi-layer, multi-channel laser coaxial powder feeding process, when the laser scans to the N+1 layer, there is a high power heat input to the already built N layer, resulting in a heat-affected zone (HAZ), which is equivalent to going through a rapid heat treatment process.The region that does not receive enough heat to allow the phase change to occur is referred to as the Unaffected area by heat (UAH).

During the experiment, it was measured that the construction height of each layer of laser coaxial powder feeding was in the range of 900-1200μm. Figure. 6(b) is a complete metallographic picture of the construction height of one layer. The construction height of a single layer is 1140.35μm, and the HAZ length is 526.32 μm, which accounts for the proportion 46.15%; UAH length is 614.03μm, accounting for 53.85%. According to Figure. 7a, it can be clearly seen that in the UAH area, the microstructure is mainly untempered lath martensite, massive,

and inclusions, in addition to the existence of prior austenite grain boundaries (PAGB). Since the transformation of austenite to martensite will cause larger lattice distortion, heat treatment is needed to eliminate it. The results of the self-tempering heat treatment obtained in the experiment are shown in Figure. 7(b), which is the UAH region we named before[20]. Microscopic observation of 9Cr steel after tempering heat treatment at 760°C showed that the entire material was homogenized and no longer distinguished between the UAH and HAZ regions as shown in Figure. 7(c). We use red parallel arrows to mark the lath martensite and the pre-austenite grain boundaries. It can be seen that there is no obvious lath martensite in the UAH area that has not undergone heat treatment, mainly prior austenite and massive martensite, and after the heat treatment process, there is basically no residual austenite, which is mainly caused by tempering. The results obtained before heat treatment in the HAZ region are almost indistinguishable from those obtained after heat treatment, with the composition of the precipitated phases such as lath martensite, δ-ferrite, $M_{23}C_6$ and MX[21]. According to the obtained microstructure image, the schematic diagram of the phase change during the tempering heat treatment process is shown in Figure. 8.

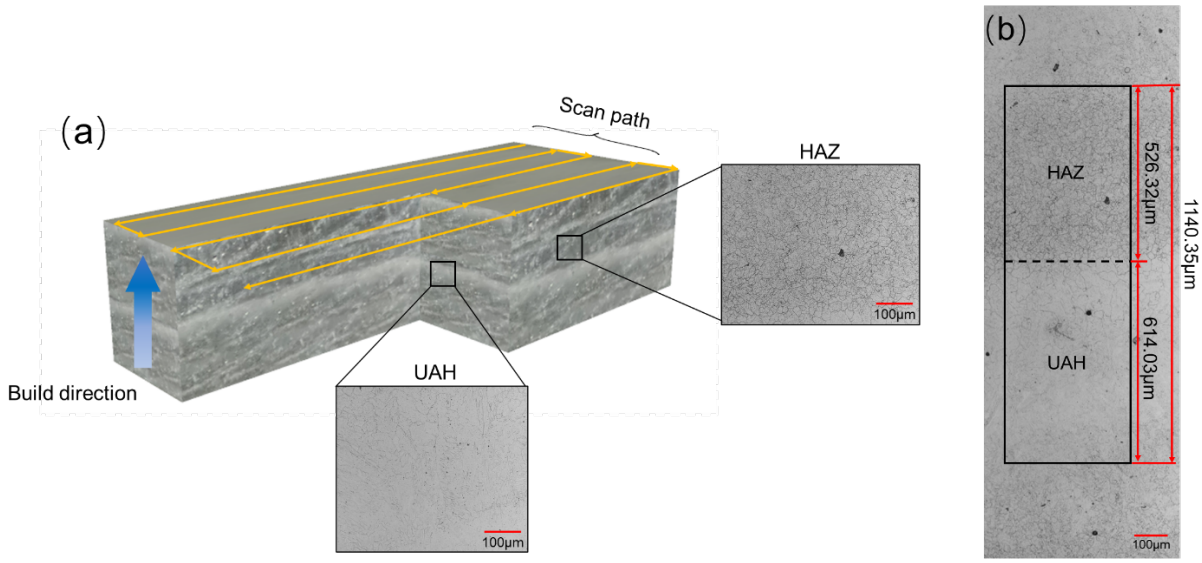

Figure. 6 (a) Macro image of 9Cr steel constructed by laser additive manufacturing, (b) HAZ and UAH area formed by the influence of N+1 layer on the nth build layer(construction direction Z) .

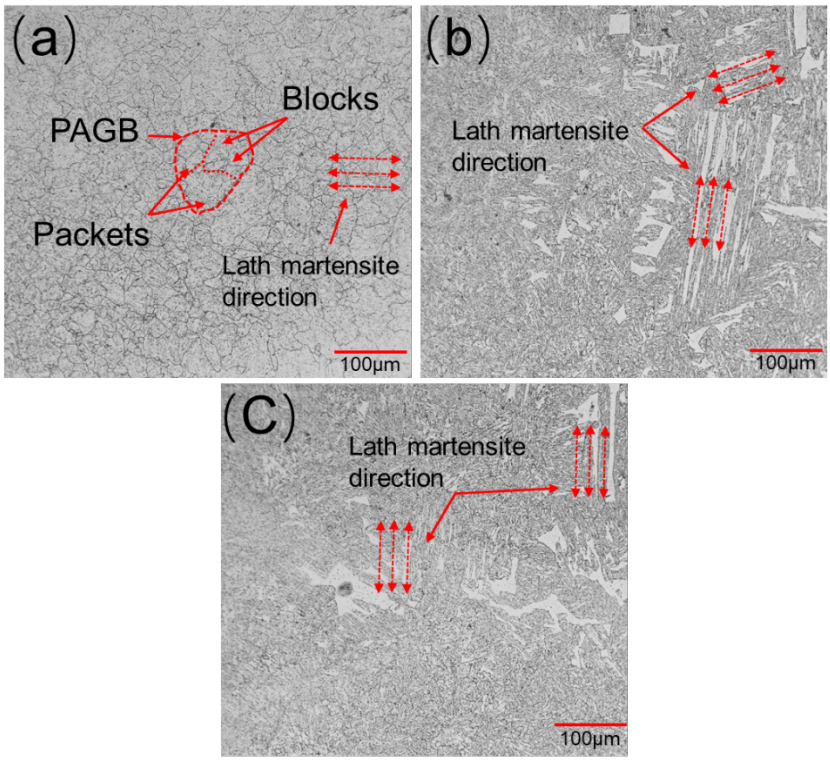

Figure. 7 Metallographic images of 9Cr steel fabricated by laser additive and its heat treatment, (a) UAH zone of 9Cr steel, (b) HAZ zone of 9Cr steel, (c) HAZ zone after tempering heat treatment.

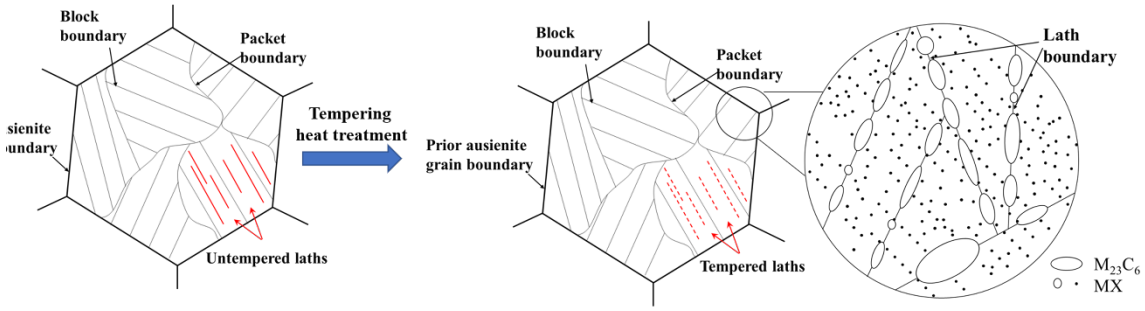

Figure. 8 Schematic diagram of the effect of heat treatment on the microstructure of 9Cr steel.

After the tempering heat treatment process, the room temperature structure obtained is mainly tempered martensite. Due to the high content of Cr in 9Cr steel, it will reduce the self-diffusion coefficient of Fe, so even in the case of slow cooling rate (Furnace cooling), when cooled to room temperature, the full martensite structure can still be obtained. After heat treatment, the alloying elements in the austenite are homogenized at high temperature, the quenched martensite is converted to tempered martensite, and some of the alloying elements are precipitated in

the form of precipitates, thereby obtaining lath martensite strengthening and dislocations. The composite strengthening mechanisms include grain refinement strengthening, solid solution strengthening and precipitation strengthening. The strengthening mechanism of lath martensite is mainly because this tempered lath martensite structure not only retains the martensite grain boundary and subgrain boundary strengthening effect, but also forms a metastable dislocation network, thereby improving thermal stability of 9Cr steel. In the enlarged image of Figure. 8, we further analyze the precipitated phase after the tempering heat treatment process. The structure is mainly composed of lath martensite matrix and dispersed precipitated phases. The larger one is $M_{23}C_6$ phase, the MX phase is mainly carbides of Ta, V and Nb. The $M_{23}C_6$ precipitates formed during the tempering heat treatment process are mainly located in the pre-austenite grains, lath boundaries, and grain boundaries[22,23]. The stable existence of $M_{23}C_6$ at grain boundaries, sub-grain boundaries and lath martensite boundaries will make 9Cr steel have good high-temperature creep properties, but with long-term creep and aging, the size of the precipitated phase M will increase, resulting in aging of 9cr steel. The MX precipitation phase is mainly nitrides or carbides precipitated by the Ta, V, and Nb elements dispersed in the crystal. The existence of X precipitates effectively inhibits the recovery process and recrystallization process of tempered martensite structure, and improves the creep properties of martensite steel[24–26]. The dispersion of MX can further strengthen the 9Cr steel, which can effectively prevent the movement of dislocations and form a dispersed phase strengthening.

Figure. 9 shows the X-ray diffraction patterns of 9Cr steel samples manufactured by laser additive with different particle sizes before and after heat treatment. According to the XRD diffraction peaks, the as-built samples consist of α'-Fe (BCC) phase and a small amount of γ'-Fe (FCC) phase. The crystallographic indices of the diffraction peaks of the α' phase match (1 1 0), (2 0 0) and (2 1 1), while the γ'-Fe phase matches (1 1 1), indicating the presence of a small amount of residual austenite in the as-built sample in addition to the martensitic phase[27,28]. The residual austenite phase is the austenite that quenching fails to transform into martensite and retains to room temperature. The inhomogeneity of the chemical composition and volume limitations prevent the phase change from complete austenite to martensite. In the as-built condition of 9Cr steel, the fresh α' phase is accompanied by 0.02-0.1 volume fraction of residual austenite, because the volume of austenite phase has to change during the transformation process, and after the vast majority of the matrix is converted to martensite, the residual part can only exist as austenite due to the space limitation[29,30]. In order to eliminate the effect of residual austenite on the properties of the samples, the as-built samples were tempered using a recrystallization temperature of 9Cr steel (760°C), while making the microstructure of the samples more homogeneous. The microstructure of the samples after heat treatment only has diffraction peaks of α'-Fe phase, i.e. The samples have

no or little residual austenite after heat treatment, which is difficult to be detected by XRD inspection means. According to the comprehensive analysis of the metallographic pictures and XRD we got before, we can draw the following conclusions, 9Cr steel underwent the following phase transformation process during the heat treatment. When the heating temperature reaches 760°C (recrystallization temperature of 9Cr steel), the alpha phase recrystallizes, the slat grains are gradually transformed into equiaxed grains, and the dislocation density decreases. In the holding stage, the continued diffusion of atoms leads to the aggregation and growth of austenite grains, and the residual cementite continues to dissolve into the austenite matrix, whose composition tends to be homogeneous.

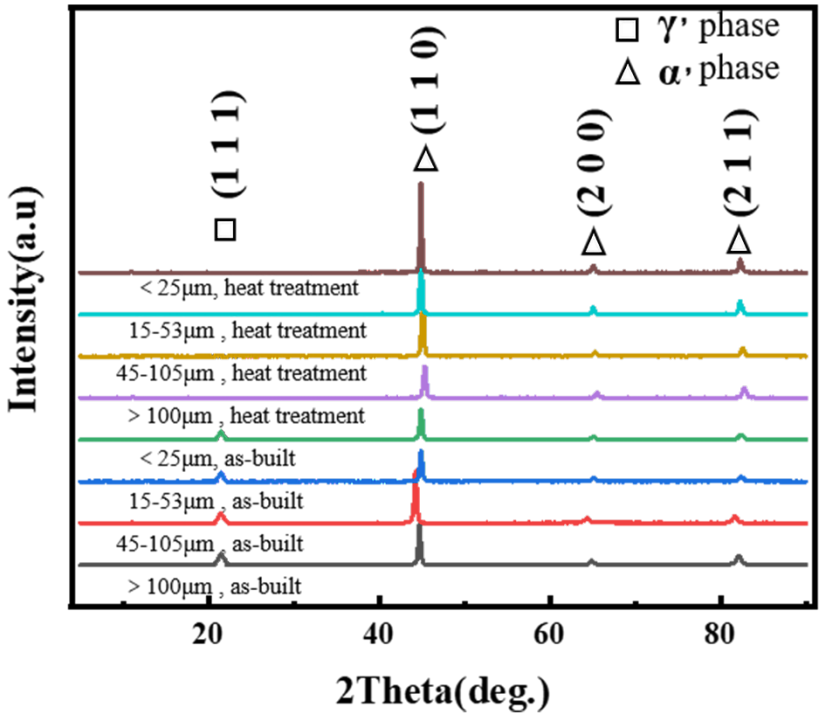

Figure. 9 XRD patterns before and after heat treatment of the powder additive samples with four particle sizes

Figure. 10 and Table 2 show the energy spectrum scan area and composition results of laser additive manufacturing of 9Cr steel. It can be seen that the element distribution of the 9Cr steel prepared by the coaxial powder feeding laser additive is similar to that of ordinary 9Cr steel, and the overall performance is homogenization, and there is no obvious segregation during the additive manufacturing process. The alloying elements often added to alloy steel are Mn, Si, Cr, Mo, W, V, Ti, Nb, Ni, Al, etc., among which Ni, Si, Al and other elements cannot form carbides with carbon, Nb, Ti, V, W, Mo, Cr, Mn and other elements can form compounds with carbon. Because alloying elements exist in steel in different forms, their roles in steel are also different. The Cr element contained in 9Cr steel accounts for about 9%. The Cr element is incorporated into the austenite, which

slows down the decomposition of the supercooled austenite, shifts the C curve to the right, reduces the critical cooling rate, and achieves the purpose of improving the hardenability[31]. Meanwhile Cr, Mn element can be made of carbide precipitation in the martensite and residual austenite decomposition temperature rises. Therefore, compared with ordinary carbon steel, the hardness and strength of alloy steel are higher than that of carbon steel when tempered at the same temperature. Conversely, when tempered to the same hardness, the tempering temperature of alloy steel is high, so the internal stress is eliminated more thoroughly, the plasticity and toughness are higher, and the tempering stability of alloy steel is improved.

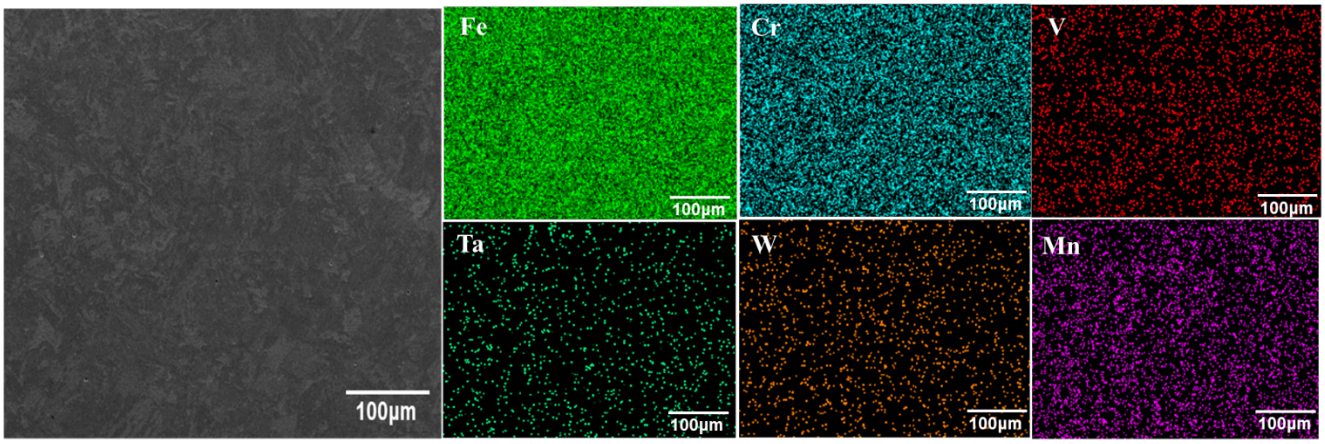

Figure. 10 As-built 9Cr steel (≤25 μm) energy spectrum scanning

Table 2 The results of energy spectrum scanning composition of 9Cr steel (≤25 μm) prepared by laser a dditive manufacturing (wt%)

Element	Fe	Cr	Ta	V	W	Si	Mn	C
Content	Bal.	9.0	0.14	0.27	1.5	0.11	0.55	0.15

In order to further compare the difference between the HAZ region and the UAH region in the as-built sample, the adoption of EBSD technique is necessary. We selected the junction of the HAZ region and the UAH region for EBSD analysis, and Figure. 11(a) shows the orientation diagram of the inverse pole figure. From the IPF plots of as-built samples, it can be seen that compared to the UAH region, HAZ region shows finer slatted martensite grains with lengths in the range of 20-40 μm and widths in the range of 0.1-3 μm, showing a narrow grain morphology. This grain size is much smaller than WAAM (200μm) or as-cast9Cr steel, which also means that the material obtains better strength and toughness, because small grain boundaries can effectively prevent the movement of dislocations in the material, the smaller the grain size, the more grain boundaries, the greater the resistance to dislocation movement, the better the strength and toughness of the material. Further, we find that the

red, blue and green colors representing {001}, {111} and {101} do not have a clear pattern of arrangement, indicating that the as-built samples do not have a clear meritocracy. Figure. 11(b) shows the Texture component of the sample, and the selected angle range is <15°. It can be found that not many Textures are obtained, which is consistent with the results analyzed in the previous inverse polar plots, and most of them are distributed in the HAZ region. Due to the advantage of fast cooling rate of laser additive itself, some of the recrystallized grains do not have time to grow and solidify in the melt pool, and are uniformly distributed near the grain boundaries as shown in Figure. 11(e) and Figure. 11(f). The polar diagram of Figure. 11(g) shows the absence of prominent strong textures in the martensite grains, a weak selective orientation at {001}, and the distribution of martensite grains in a more homogeneous form in the samples.

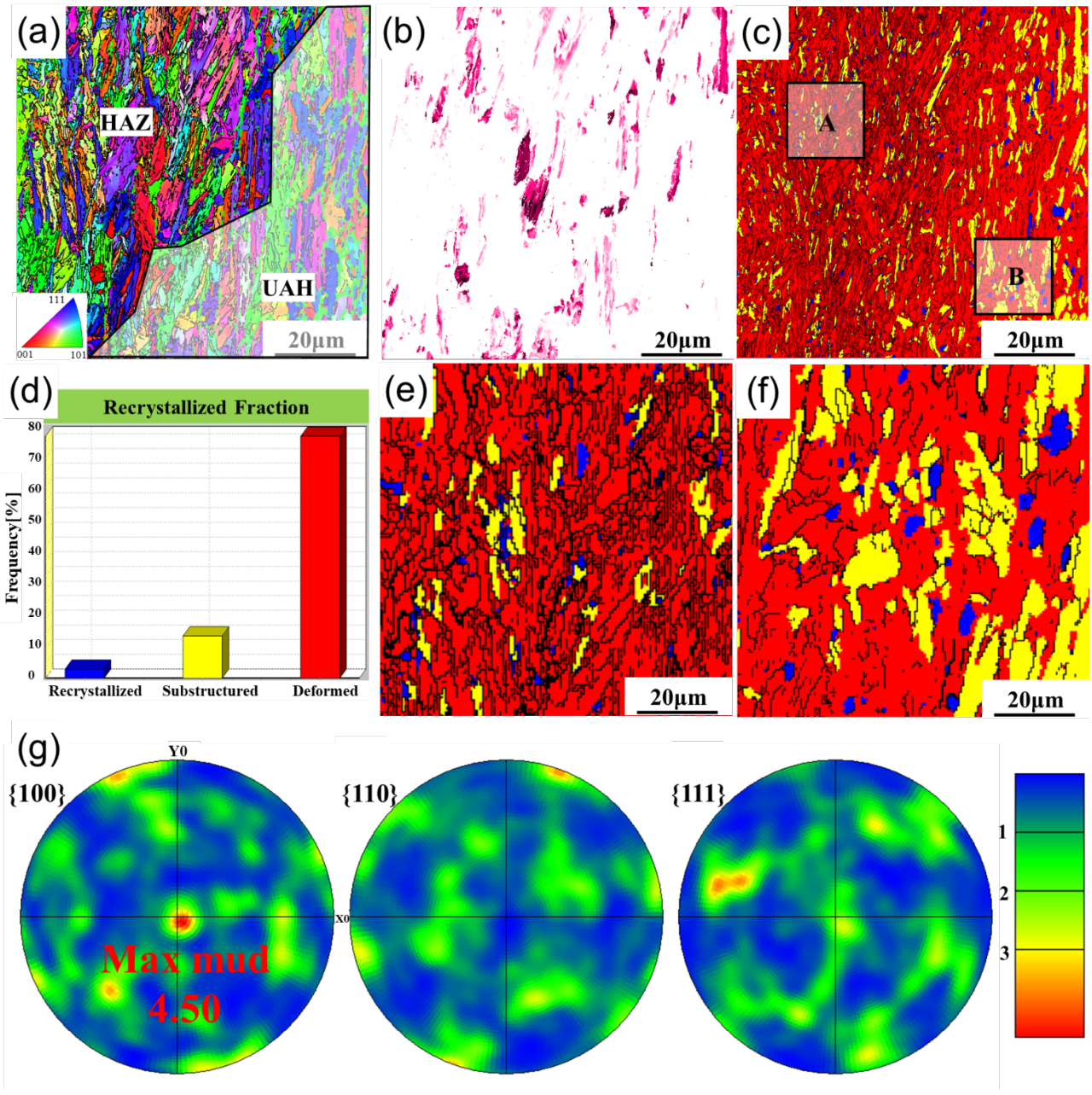

Figure. 11 EBSD image containing HAZ region and UAH region:(a) Orientation diagram of the inverse pole figure, (b) Texture component of the sample, (c) Distribution map of recrystallized fraction, (d) Histogram distribution of recrystallized fraction, (e) Magnification view of region A in figure(c), (f) Magnification view of region B in figure(c), (g) Pole figure of the sample.

The grain size and the width of the martensite lath are the main factors that affect the grain boundary or the lath grain boundary. Figure. 12 is the EBSD analysis of 9Cr steel with different grain sizes along the construction direction, reflecting the grain orientation of the material, Figure.13 is the grain size distribution diagram obtained by the EBSD analysis test, reflecting the influence of heat treatment and different grain sizes on the grain size. Figure. 12(i) is an orientation triangle, different colors represent different crystal grain directions. Red represents the crystal particle surface direction parallel to [111], blue represents the crystal particle surface direction parallel to [001] and the green crystal particle surface direction parallel to [101]. Figures. 12(a) and Figures. 12(e) represent 9Cr steels with powder additives smaller than 25μm before and after heat treatment. It can be clearly seen that the lath martensite before heat treatment has a narrow and long shape, but the ratio between length and width is small and the overall grain size Is larger, and the aspect ratio of the grains is obviously increased after heat treatment, the overall lath martensite becomes narrower and longer, and the grain size is also greatly reduced, according to Figure. 13, the grain size is reduced from 2.826μm before heat treatment to 1.820μm after heat treatment, a reduction of 35.59%. Comparing the EBSD images before and after heat treatment of 9Cr steel with four particle size powder additives, it is found that there is no obvious texture orientation, indicating that the material has an overall homogeneous characteristic along the building direction. According to the results in Figure. 8, it can be found that the martensite has a certain degree of dislocation entanglement, and heat treatment can reduce the residual stress to a certain extent. The GOS value of the grains is lower than that before the heat treatment, and the average GOS of the grains can be Expressed as:

$$GOS(i) = \sum_j \omega ij/J(i) \qquad (1)$$

where ωij represents the misorientation angle between the orientation of pixel j and the mean orientation of grain i, and J(i) is the pixel number of grain i. The GOS value of grains implies the residual stress in the grain leading to grain distortions[32,33]. According to Figure.12, there is a very high residual stress in most grains, especially in martensite grains with a higher dislocation density. In the homogenization heat treatment process, the driving force for recrystallization comes from the residual stress and the grain coarsening effect caused by the homogenization heat is closely related. There is a competition between recrystallization and grain coarsening, therefore, in order to obtain more refined grains, we need a longer heat treatment time to ensure refined grains and

less residual stress. From Figure. 13 we can draw the influence of the particle size of the additive powder on the grain size. We found that the resulting powders with particle sizes of 15-53 μm had the smallest average particle size of 1.782 μm, followed by 45-105 μm and >100 μm, and samples obtained by LMD additive manufacturing.

The grain size of the samples produced by LMD additive manufacturing of powders with a particle size of <25 μm is the largest. But at the same time, the heat treatment process has the greatest influence on its grain refinement, reaching 35.59%.The refined grain size after heat treatment is similar to the samples with other particle size additives. It can be inferred that the process of recrystallization occurred during the heat treatment process. By heating the metal to a temperature above the recrystallization temperature and keeping it for an appropriate period of time, the recrystallization can achieve the goal of homogenization of the structure, elimination of residual stress and grain refinement.

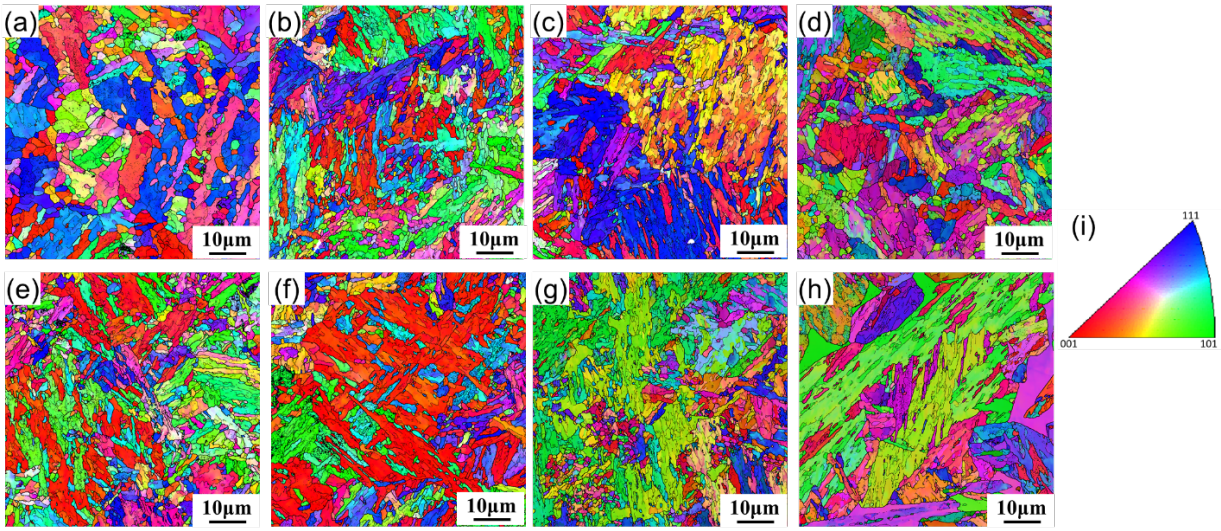

Figure. 12. Inverse pole diagrams of EBSD before and after heat treatment of the powder additive samples with four particle sizes: (a) as-built, <25 μm (b) as-built, 15-53 μm (c) as-built, 45 -105 μm (d) as-built, >100 μm (e) heat treatment, <25 μm (f) heat treatment, 15-53 μm (g) heat treatment, 45 -105 μm (h) heat treatment, >100 μm.

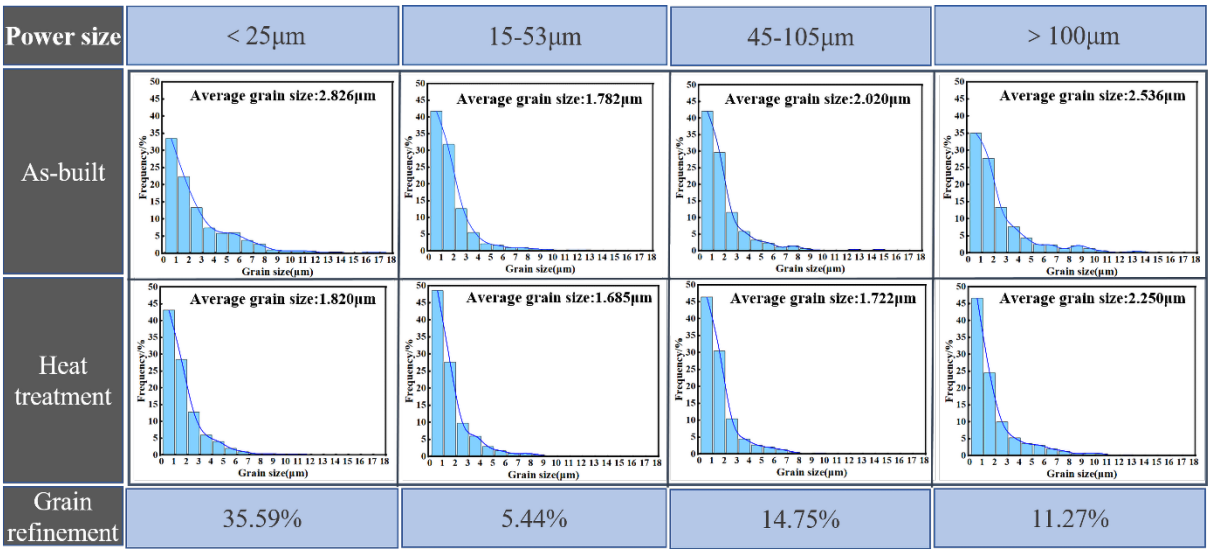

Figure.13. Average grain size before and after heat treatment of the powder additive samples with four particle sizes

3.2 Mechanical properties

3.2.1 Charpy impact property

Figure. 14 shows the Charpy impact absorbed energy (IAE) of 9Cr steel manufactured by laser with different particle sizes before and after heat treatment. The maximum impact absorbed energy of the specimen without heat treatment is less than 15 J, which is significantly lower than that of CLAM forged at room temperature (>200 J)[34], but after heat treatment, the maximum IAE of the specimen is greatly increased, reaching 100 J, We can draw the conclusion that heat treatment can greatly improve the IAE of the sample. At the same time, we compare it horizontally and find that the IAE fluctuates little before heat treatment, only the IAE of the powder additive samples >100μm is slightly larger, which may be caused by the internal pore structure; after heat treatment, the IAE gradually decreases with the increase of the powder particle size, in order to explore the reasons, further analysis of its fracture.

Figure. 15 is a microscopic image of the fracture image of the impact test. The fracture of the heat-treated sample exhibits significantly different fracture characteristics. The powder additive samples with a particle size of <25 μm exhibited trans-crystalline mode failure, showing lamellar hyoid fracture, and the powder additive samples with a particle size of >100 μm exhibited intergranular dominant mode failure, with mixed characteristics of quasi-dissociation and pits. Obvious pore structure can be observed at the impact fracture of the powder additive with a particle size of >100 μm, which can improve the IAE to a certain extent, but the overall is still not high. The impact fractures of samples <25 μm and 15-53 μm are all small dimple structures, while the impact fractures of samples

45-105 μm show shear fracture dimples. Its shape is affected by the impact load, when the sample is broken and torn, it receives the action of the moment, and the shear stress is different before the microscopic cavity gathers, and the amount of plastic deformation caused is also different. The dimples in the larger direction (the tearing direction) are elongated and present a parabolic shape, as shown in Figure. 15(c). The heat treatment greatly improves the IAE of the sample, mainly because the crystal grains boundaries prevent the cracks from propagating along the weld line, thereby improving the impact toughness of the material.

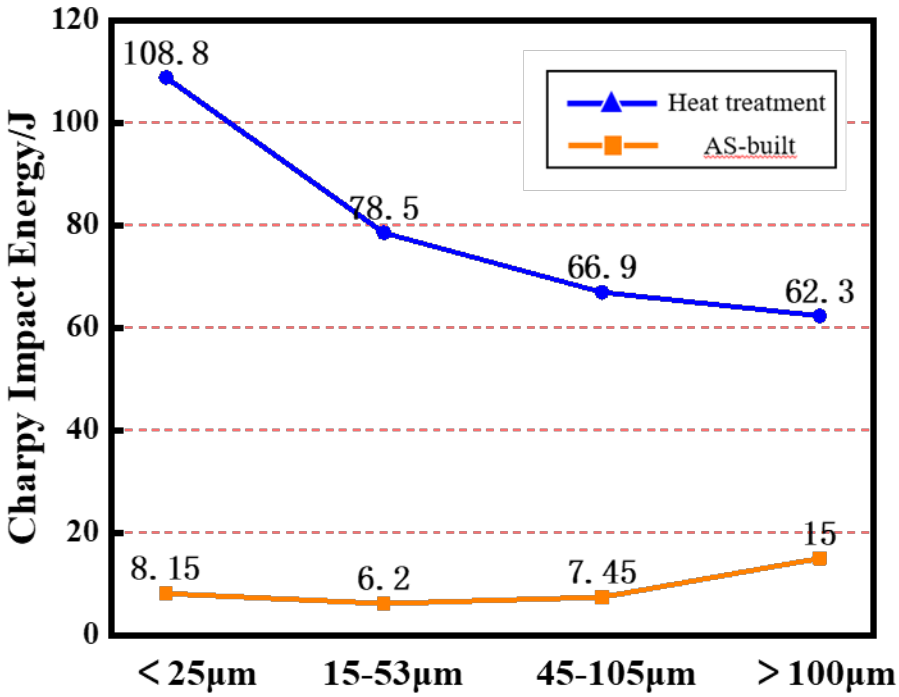

Figure. 14. Charpy impact energy of 9Cr steel before and after heat treatment of the powder additive samples with four particle sizes

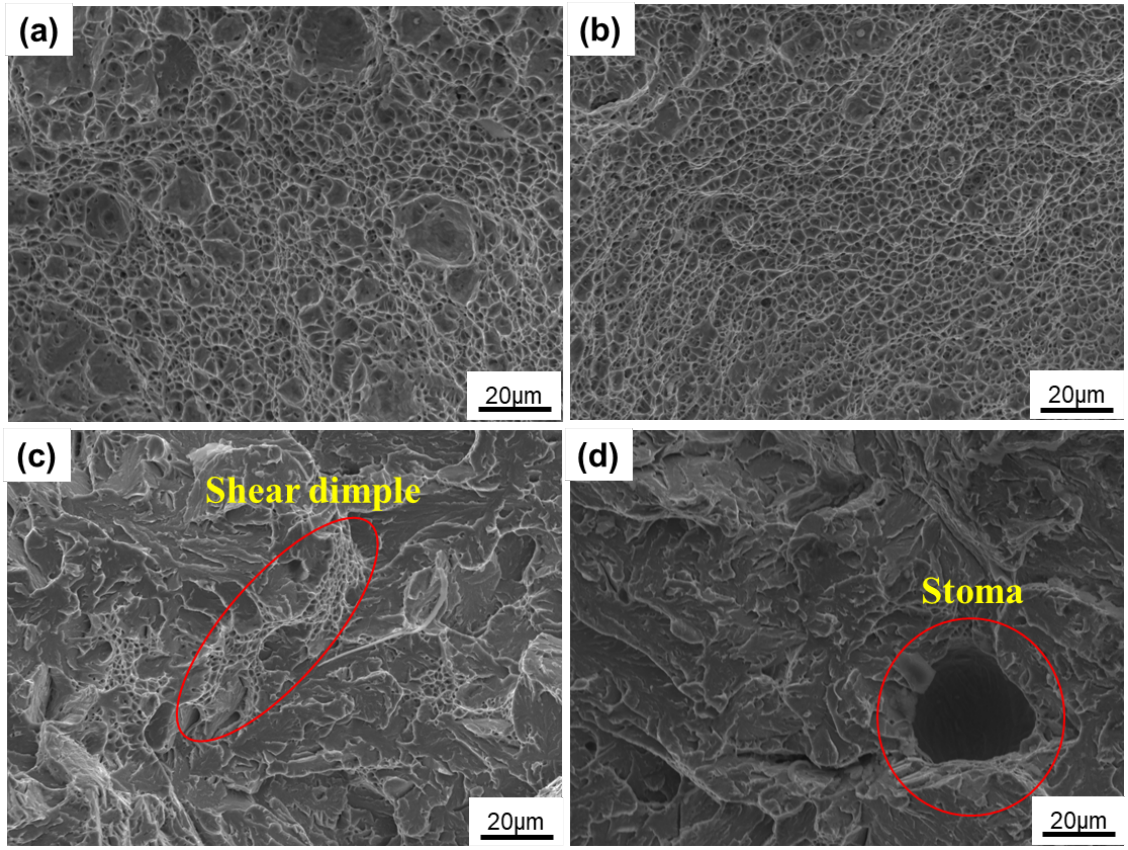

Figure. 15. Impact fracture image of heat-treated specimen: (a) <25 μm (b) 15-53 μm (c) 45 -105 μm (d) >100 μm.

3.3.2 Tensile property

Tensile tests were performed on 9Cr steel samples manufactured by adding powders of different particle sizes before and after heat treatment. The test results are shown in Figure. 16. As the particle size of the powder increases, the tensile strength increases to a certain extent. Compared with the ultimate tensile strength of forged CLAM, almost all 9Cr steel specimens constructed by LMD can reach ultimate tensile strength (UTS)> 650 MPa. The tensile strength of the 9Cr steel sample with the powder particle size of 45-105μm can reach 1057.7MPa, which is 62.7% higher than the cast 9Cr steel, but the elongation is 9.21%, which is slightly smaller than the cast 9Cr steel. The 9Cr steel manufactured by LMD additive has a faster cooling rate, and the formed structure is quenched martensite. The structure is partially heated and tempered in the later n+1 layer construction, which is the HAZ area we mentioned in the previous section. Therefore, even if there are defects, it has higher hardness and strength than conventionally manufactured 9Cr using standard heat treatment. When the entire sample is tempered and heat treated, the UAH area disappears and all becomes the HAZ area, and the overall grain size also decreases. However, we found that the tensile strength did not increase, but decreased. Depending on the particle size, heat treatment reduces the tensile strength of the sample by 15%-21%, which is inconsistent with the strength improvement we previously expected.

In order to find out the reason for the change in tensile strength, we observed the fracture morphology, as shown in Figure. 17. According to the fracture morphology, in terms of molding, when the particle size of the powder is small (<25 μm, 15 -53 μm), there will be no defects such as pores and cracks in tensile fracture, and the moldability is good, as shown in Figure. 17(a), Figure. 17(c). On the other hand, there are more pores in samples with larger powder particle size (45-105 μm, >100 μm), especially the >100 μm sample has a very large porosity, and the maximum pore size can reach 40 μm, as shown in Figure. 17(e), Figure. 17(g). As the particle size of the powder increases, the dimples gradually become larger and deeper, and the tensile strength gradually increases. However, due to the large pores in the 100-micron sample, the tensile strength decreases. In general, the main fracture mechanism of the sample before heat treatment is ductile fracture, and the average size of the pits is similar to the size of the honeycomb grains of 9Cr steel, which is found in the work of Zhang et al[35]. When the density of the block reaches a high level (≥98%), according to the grain boundary strengthening theory, because a large number of grain boundaries hinder the movement of dislocations, the grain size becomes the most important factor affecting the tensile strength[36]. Therefore, the high tensile strength obtained can be attributed to the small cell size of porous dendrites (0.3 to 1.4 μm), which is different from traditional strengthening methods (such as work hardening). The traditional strengthening method increases the strength of the material at the expense of ductility, while the 9Cr steel made by LMD is reinforced without loss of ductility.

The tensile fractures of the sample after heat treatment are shown in Figure. 16(b), 16(d), 16(f), 16(g). We can find that compared with before heat treatment, there are almost no dimples, even small dimples. After the surface heat treatment, the main fracture mode is cleavage fracture, which has a typical river-type fracture surface. Some of the intergranular fracture characteristics along the grains are obvious, as shown by the red arrows. The different orientations of the river grain mean different orientations of martensite blocks in the finished sample. At high magnification, it is obvious that part of the precipitate is bare or embedded in the crack wall. According to the above characterization results, this is the MX phase. Heat treatment leads to a decrease in tensile strength which main reason is that tempered martensite loses dislocation density and supersaturation of elements such as Cr, W and C during the heat treatment process, which Weakened the solid solution strengthening effect caused by high-density dislocations in homogeneous martensite. The EDS analysis of the composition on point 1 is given in Figure. 17. Although the particle is too small for precise measurements, the precipitate is enriched in Nb, which can be confirmed as MX in the thermodynamic model predictions (Figure. 3a).

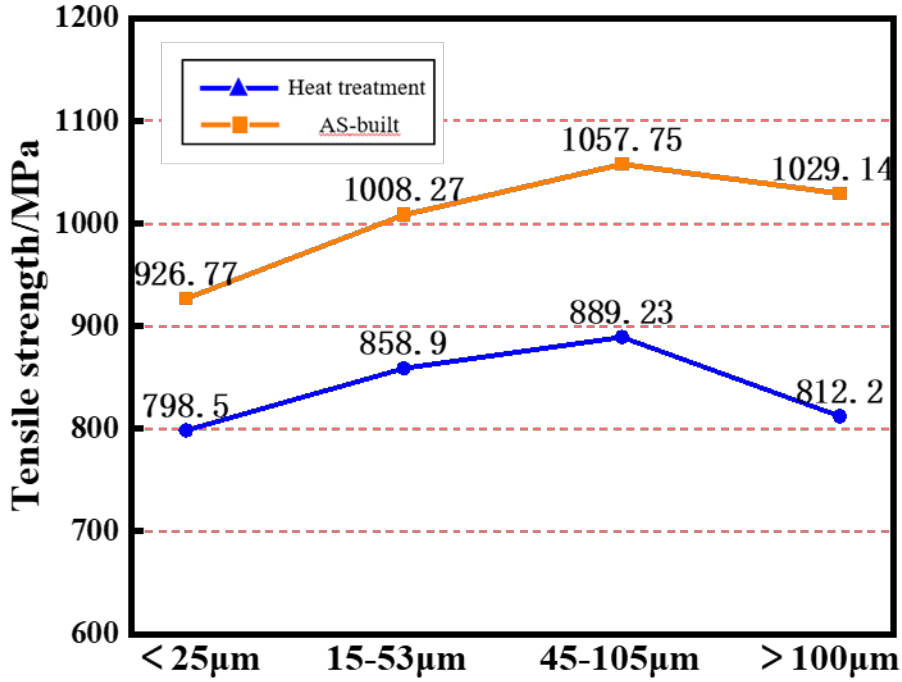

Figure. 16. Tensile strength of 9Cr steel before and after heat treatment of the powder additive samples with four particle sizes

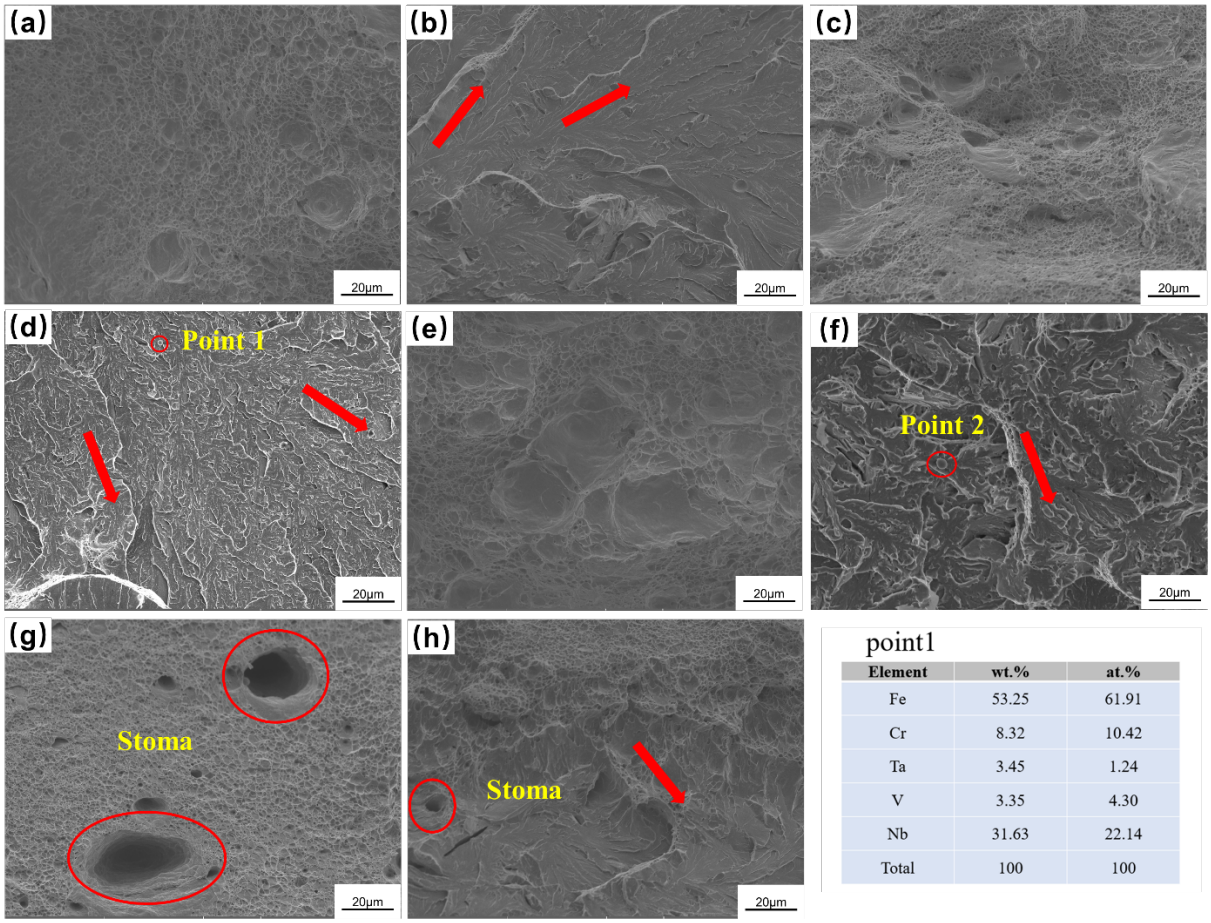

point1

Element	wt.%	at.%
Fe	53.25	61.91
Cr	8.32	10.42
Ta	3.45	1.24
V	3.35	4.30
Nb	31.63	22.14
Total	100	100

Figure. 17 Microscopic image of tensile fracture before and after heat treatment of the powder additive samples with four particle sizes:(a) as-built, <25 μm (b) heat treatment, <25 μm (c) as-built, 15-53 μm (d) heat treatment, 15-53 μm (e) as-built, 45 -105 μm (f) heat treatment, 45 -105 μm (g) as-built, >100 μm (h) heat treatment, >100 μm.

3.2.3 Microscopic Vickers hardness

We tested the microhardness of 8 samples in the vertical and horizontal directions, as shown in Figure. 18. The load applied in the hardness test is 300 g, and the load holding time is 10 s. A hardness test point is made every 0.1 mm, and the transverse (perpendicular to the weld) and longitudinal (parallel to the weld) hardness of 8 specimens are measured. We selected the one in the HAZ area in the longitudinal direction, in order to further observe the fluctuation of the hardness in the HAZ area.It can be found that the horizontal measured hardness value fluctuates less, and it is basically equal to the longitudinal peak hardness, that is, the hardness of the HAZ area is greater than UAH, and the self-heating effect of the LMD process has a certain increase in the hardness value.

According to the horizontal and vertical comparative analysis, 15-53 μm and 45-105 μm samples have the highest hardness, which is the smallest average grain size of these two powders, resulting in higher hardness. The samples >100 μm have many defects, such as pores, cracks, etc., which lead to large fluctuations in their hardness.

In the transverse hardness chart (16b), there is a low hardness value, which is the Vickers hardness value measured around the pore. Poor microhardness indicates that porosity has a great influence on microhardness, because the pores inside the material collapse under load[37]..

Let's take a look at the effect of the heat treatment process on the hardness. We found that compared to the as-built sample, the heat treatment resulted in a greater reduction in the hardness, from about 330Hv to 220Hv. There are also some MX precipitates in the heat treatment process, which have a Zenner pinning effect on grain refinement. However, the volume fraction and size of MX are extremely small, so compared with the solid solution strengthening effect produced by the high density of dislocations in homogeneous martensite, the effect of MX on strengthening is not obvious. Tempering heat treatment reduces hardness and improves plasticity to facilitate cutting. This is because air cooling is used after hot working. Due to the faster cooling rate, the structure is dispersed or martensite is obtained, so the hardness is also higher, especially for alloy steel. After annealing, the hardness can be reduced, which is conducive to cutting.

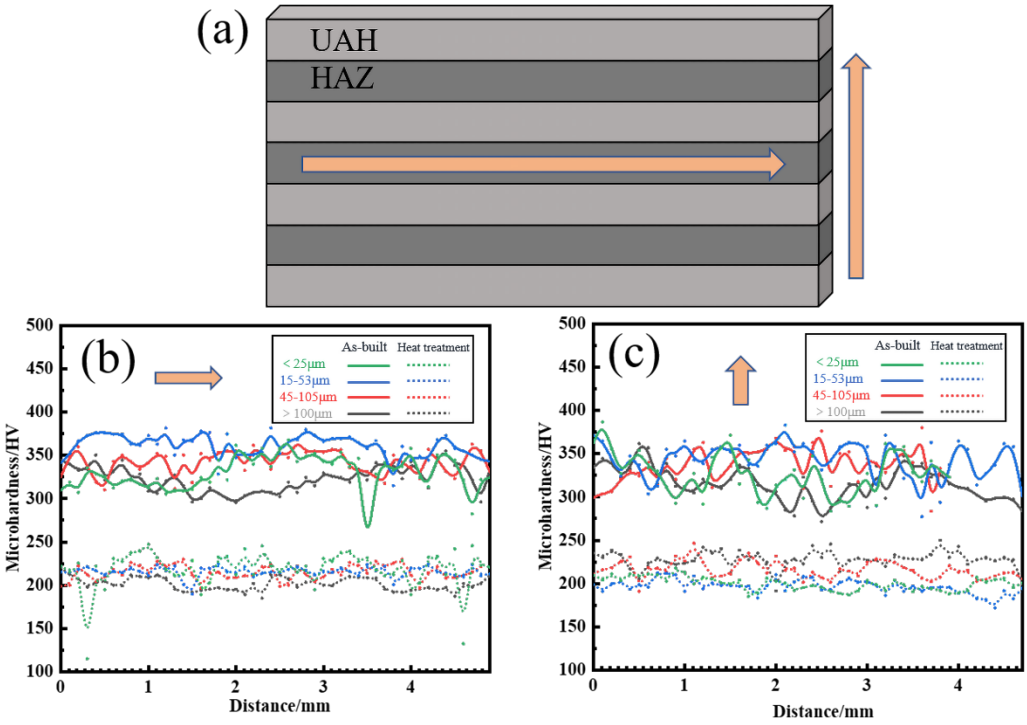

Figure. 18. Microhardness before and after heat treatment of the powder additive samples with four particle sizes, (a)Schematic diagram of hardness selection point distribution (b) parallel to the scanning direction (HAZ zone), (c) perpendicular to the scanning direction

3.3 Nanoindentation

In order to further characterize the difference in mechanical properties between the precipitated phase and the

uniform state, we selected the area with the precipitated phase after the heat treatment to perform the nanoindentation test, as shown in Figure. 19. We start with a precipitated phase (M region) as a starting point, and set a rectangular lattice pattern for nanoindentation Figure. 19(a) to compare the difference in micromechanical properties nearby. We selected four regions of data for further analysis, namely M region (on the precipitated phase), N region (near the precipitated phase), W phase (a little far away from the precipitated phase), and R region (no precipitated phase), the load-displacement curve obtained is shown in Figure. 19(c). Under the same load condition (10mN), the indentation depth in the M region is the deepest, the indentation depth in the N region is the second deepest, the indentation depth in the W region is the third deepest, and the indentation depth in the R region is the smallest which data results are consistent with the data of other non-precipitated phase regions. Therefore, the precipitated phase in the W area is softer than the normal area, and the difference in the nano-hardness of the three phases can be reflected by the indentation size effect (ISE) [38,39], this indicates that the decrease in the size of the indentation leads to an increase in nano-hardness and a decrease in plasticity. Calculate the elastic modulus and nanoindentation of each area by the Oliver-Pharr method, and the calculated results are shown in Figure. 19. The elastic modulus of the M region (precipitated phase) is 104.250 GPa, which is much lower than the 168.192 GPa of the R region. After analyzing the elastic modulus of the N region and W region, it is found that the closer to the precipitated phase, the lower the elastic modulus. It shows that the precipitation has a negative effect on the relative elastic modulus, but this is not obvious in the hardness change, the nano-hardness values of the M region, the N region, and the W region have little difference. We further conducted elemental analysis of the precipitated phase in the M region and found that the precipitated phase is rich in Fe, Cr, and C elements, and combined with its size (5-8μm), the precipitated phase is determined to be $M_{23}C_6$. The precipitation of $M_{23}C_6$ precipitated phase at the grain boundary will harden the material to a certain extent, but the elastic modulus and nano-hardness of the precipitated phase will be lower than that of the uniform phase to a certain extent.

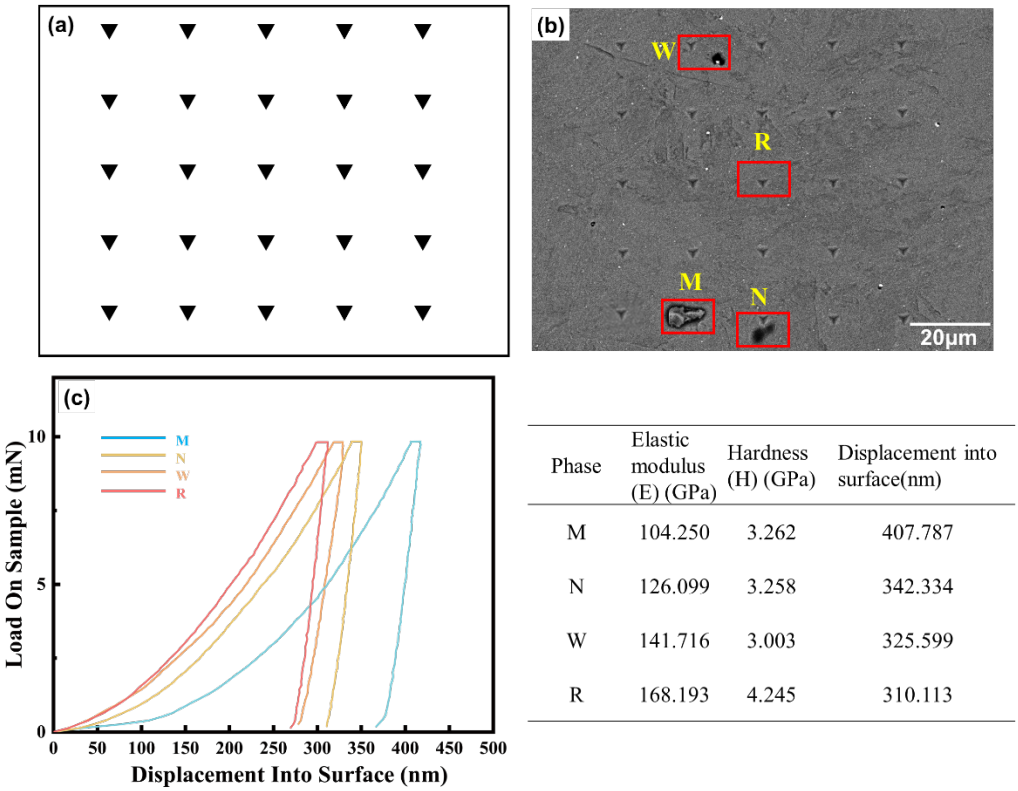

Phase	Elastic modulus (E) (GPa)	Hardness (H) (GPa)	Displacement into surface(nm)
M	104.250	3.262	407.787
N	126.099	3.258	342.334
W	141.716	3.003	325.599
R	168.193	4.245	310.113

Figure. 19. Nanoindentation test of heat-treated samples: (a) Rectangular lattice pattern of nanoindentation, (b) SEM image of nanoindentation, (c) Load-displacement graph and elastic modulus, nano-hardness, and indentation depth data

4. Conclusion

For the first time, the effects of laser coaxial powder feeding additive 9Cr steel and post heat treatment on the microstructure and mechanical properties are studied with the help of heat treatment simulation. The main conclusions are summarized as follows:

(1) Using four powder sizes (<25 μm, 15-53 μm, 45 -105 μm, >100 μm), a high-density 9Cr steel block structure was successfully prepared by laser coaxial powder feeding. The construction of 9Cr steel has obvious stratification along the construction direction, and there are UAH and HAZ divisions in the single-story layer. In UAH, there are mainly prioraustenite and lath martensite, and massive martensite exists. There is almost no retained austenite in the HAZ zone the results are similar to the results of our heat treatment samples. The main microstructure is tempered lath martensite, ferrite, MX and other precipitated phases. Before and after heat treatment, the structure has no obvious texture orientation, and the whole sample is homogeneous. The grain size of the samples produced by LMD additive manufacturing of powders with a particle size of <25 μm is the largest. But at the same time, the heat

treatment process has the greatest influence on its grain refinement, reaching 35.59%.

(2) The reheat input of laser energy to the HAZ region leads to grain refinement and a tendency for the recrystallized grains to develop a texture. HAZ region shows finer slatted martensite grains with lengths in the range of 20-40 μm and widths in the range of 0.1-3 μm, showing a narrow grain morphology. This grain size is much smaller than WAAM (200μm) or as-cast9Cr steel, which also means that the material obtains better strength and toughness. The maximum tensile strength of the built sample is 1057.75 MPa, which is much greater than the 650 MPa of standard cast 9Cr steel. There are two types of fracture mechanisms: ductile fracture and mixed fracture. The heterogeneous structure leads to uneven fracture. After heat treatment, the entire sample has a homogeneous structure with a small decrease in tensile strength, but the plasticity is improved compared to the built-up sample.

(3) After 9Cr steel is tempered at 760°C, the average grain size is reduced, the Charpy impact performance is greatly improved, but the tensile strength is slightly reduced, and the MicroVickers hardness is also reduced to a certain extent. The main reason is that during the tempering heat treatment, the high dislocation density of lath martensite is greatly reduced, and the supersaturation behavior of Cr, W, and C elements weakens the effect of solid solution strengthening.

(4) Through the nanoindentation test, we found that the elastic modulus (104.250GPa) of the precipitated $M_{23}C_6$ phase is much lower than that of the homogeneous phase (168.192GPa). The closer the precipitates phase, the lower the elastic modulus. The precipitation of the $M_{23}C_6$ precipitated phase at the grain boundary will harden the material to a certain extent, but at the microscopic level, its elastic modulus and nano-hardness are lower than that of the homogeneousphase.

Acknowledgements

This research was supported by Foundation of Natural Science Foundation of China (52075317), Science Foundation of Institute of Plasma Physics Chinese Academy of Sciences (No. DSJJ-18-01), the Royal Society through International Exchanges 2018 Cost Share (China) scheme (IEC\NSFC\181278), Shanghai Science and Technology Committee Innovation Grant (19511106400, 19511106402), Shanghai Local Colleges and Universities Capacity Building Special Plan Project (19030501300).

References

[1] C. Cabet, F. Dalle, E. Gaganidze, J. Henry, H. Tanigawa, Ferritic-martensitic steels for fission and fusion applications, Journal of Nuclear Materials. 523 (2019) 510–537. https://doi.org/10.1016/j.jnucmat.2019.05.058.

[2] S. Li, X. Yang, N. Vajragupta, W. Tang, A. Hartmaier, H. Li, The influence of post-weld tempering

temperatures on microstructure and strength in the stir zone of friction stir welded reduced activation ferritic/martensitic steel, Materials Science and Engineering: A. 814 (2021) 141224. https://doi.org/10.1016/J.MSEA.2021.141224.

[3] D. Wu, S. Wei, S. Lu, A Study of Microstructure and Mechanical Properties for the Autogenous Single-Pass Butt Weldment of a Ferritic/Martensitic Steel Using Gas Tungsten Arc Welding, Acta Metallurgica Sinica (English Letters). 34 (2021) 628–638. https://doi.org/10.1007/s40195-020-01146-5.

[4] A. Lanzutti, F. Andreatta, M. Lekka, L. Fedrizzi, Microstructural and local electrochemical characterisation of Gr. 91 steel-welded joints as function of post-weld heat treatments, Corrosion Science. 148 (2019) 407–417. https://doi.org/10.1016/j.corsci.2018.12.042.

[5] K. Zhang, J. Aktaa, Characterization and modeling of the ratcheting behavior of the ferritic-martensitic steel P91, Journal of Nuclear Materials. 472 (2016) 227–239. https://doi.org/10.1016/j.jnucmat.2015.10.050.

[6] Q. Wu, S. Zheng, S. Liu, C. Li, Q. Huang, Effect of post-weld heat treatment on the mechanical properties of electron beam welded joints for CLAM steel, Journal of Nuclear Materials. 442 (2013) 512–517. https://doi.org/10.1016/j.jnucmat.2013.07.041.

[7] Z. Jiang, L. Ren, J. Huang, X. Ju, H. Wu, Q. Huang, Y. Wu, Microstructure and mechanical properties of the TIG welded joints of fusion CLAM steel, Fusion Engineering and Design. 85 (2010) 1903–1908. https://doi.org/10.1016/j.fusengdes.2010.06.019.

[8] Y. Lei, C. Xiao, X. Wang, J. Yue, Q. Zhu, Tensile properties and fracturing behavior of weld joints in the CLAM at high temperatures, Fusion Engineering and Design. 95 (2015) 27–33. https://doi.org/10.1016/j.fusengdes.2015.04.002.

[9] M. Jiang, C. Liu, Z. Chen, P. Wang, H. Liao, D. Zhao, Z. Liu, X. Wang, M. Xu, C. Lao, Enhanced strength-ductility synergy of selective laser melted reduced activation ferritic/martensitic steel via heterogeneous microstructure modification, Materials Science and Engineering A. 801 (2021) 140424. https://doi.org/10.1016/j.msea.2020.140424.

[10] Y. Zhai, B. Huang, X. Mao, M. Zheng, Effect of hot isostatic pressing on microstructure and mechanical properties of CLAM steel produced by selective laser melting, Journal of Nuclear Materials. 515 (2019) 111–121. https://doi.org/10.1016/j.jnucmat.2018.12.028.

[11] B. Huang, Y. Zhai, S. Liu, X. Mao, Microstructure anisotropy and its effect on mechanical properties of reduced activation ferritic/martensitic steel fabricated by selective laser melting, Journal of Nuclear Materials. 500 (2018) 33–41. https://doi.org/10.1016/j.jnucmat.2017.12.011.

[12] C. Gao, X. Chen, X. Chen, C. Su, Materials Science and Technology Microstructure and mechanical properties of as-deposited and heat-treated additive manufactured 9Cr steel Microstructure and mechanical properties of as-deposited and heat-treated additive manufactured 9Cr steel, MATERIALS SCIENCE AND TECHNOLOGY. 35 (2019) 2234–2242. https://doi.org/10.1080/02670836.2019.1668603.

[13] A.V. Nemani, M. Ghaffari, A. Nasiri, materials On the Post-Printing Heat Treatment of a Wire Arc Additively Manufactured ER70S Part, (n.d.). https://doi.org/10.3390/ma13122795.

[14] A. Chatterjee, A. Moitra, A.K. Bhaduri, D. Chakrabarti, R. Mitra, Effect of Heat Treatment on Ductile-Brittle Transition Behaviour of 9Cr-1Mo Steel, Procedia Engineering. 86 (2014) 287–294. https://doi.org/10.1016/J.PROENG.2014.11.040.

[15] S.A. Maloy, T.A. Saleh, O. Anderoglu, T.J. Romero, G.R. Odette, T. Yamamoto, S. Li, J.I. Cole, R. Fielding, Characterization and comparative analysis of the tensile properties of five tempered martensitic steels and an oxide dispersion strengthened ferritic alloy irradiated at ≈295 °C to ≈6.5 dpa, Journal of Nuclear Materials. 468 (2016) 232–239. https://doi.org/10.1016/J.JNUCMAT.2015.07.039.

[16] M. Song, C. Sun, Z. Fan, Y. Chen, R. Zhu, K.Y. Yu, K.T. Hartwig, H. Wang, X. Zhang, A roadmap for tailoring the

strength and ductility of ferritic/martensitic T91 steel via thermo-mechanical treatment, Acta Materialia. 112 (2016) 361–377. https://doi.org/10.1016/J.ACTAMAT.2016.04.031.

[17] C. Pandey, A. Giri, M.M. Mahapatra, Evolution of phases in P91 steel in various heat treatment conditions and their effect on microstructure stability and mechanical properties, Materials Science and Engineering A. 664 (2016) 58–74. https://doi.org/10.1016/j.msea.2016.03.132.

[18] L. Hu, X. Wang, Q. Ma, W. Meng, S. Chen, Numerical and experimental investigations on the temperature field in local post weld heat treatment of 9 % Cr heat resistant steel welded pipes, Journal of Materials Processing Technology. 297 (2021). https://doi.org/10.1016/j.jmatprotec.2021.117232.

[19] S. Kumar, V. Yadav, S. Sharma, C. Pandey, A. Goyal, P. Kumar, Role of dissimilar Ni-based ERNiCrMo-3 filler on the microstructure, mechanical properties and weld induced residual stresses of the ferritic/martensitic P91 steel welds joint, International Journal of Pressure Vessels and Piping. 193 (2021). https://doi.org/10.1016/j.ijpvp.2021.104443.

[20] S.A.O. Nair, R.G. Pillai, Microstructural and corrosion characteristics of Quenched and Self-Tempered (QST) steel reinforcing bars, Construction and Building Materials. 231 (2020) 117109. https://doi.org/10.1016/J.CONBUILDMAT.2019.117109.

[21] F. Abe, Precipitate design for creep strengthening of 9% Cr tempered martensitic steel for ultra-supercritical power plants, in: Science and Technology of Advanced Materials, 2008. https://doi.org/10.1088/1468-6996/9/1/013002.

[22] R.L. Klueh, A.T. Nelson, Ferritic/martensitic steels for next-generation reactors, Journal of Nuclear Materials. 371 (2007) 37–52. https://doi.org/10.1016/j.jnucmat.2007.05.005.

[23] Q. Lu, W. Xu, S. van der Zwaag, The Computational Design of W and Co-Containing Creep-Resistant Steels with Barely Coarsening Laves Phase and M23C6as the Strengthening Precipitates, Metallurgical and Materials Transactions A: Physical Metallurgy and Materials Science. 45 (2014) 6067–6074. https://doi.org/10.1007/s11661-014-2557-x.

[24] T. Shrestha, M. Basirat, I. Charit, G.P. Potirniche, K.K. Rink, U. Sahaym, Creep deformation mechanisms in modified 9Cr-1Mo steel, Journal of Nuclear Materials. 423 (2012) 110–119. https://doi.org/10.1016/j.jnucmat.2012.01.005.

[25] P.R. Kalvala, J. Akram, M. Misra, D. Ramachandran, J.R. Gabbita, Low temperature friction stir welding of P91 steel, Defence Technology. 12 (2016) 285–289. https://doi.org/10.1016/j.dt.2015.11.003.

[26] N. Saini, R.S. Mulik, M.M. Mahapatra, Influence of filler metals and PWHT regime on the microstructure and mechanical property relationships of CSEF steels dissimilar welded joints, International Journal of Pressure Vessels and Piping. 170 (2019) 1–9. https://doi.org/10.1016/j.ijpvp.2019.01.005.

[27] C. Wang, Y. Chen, J. Han, D. Ping, X. Zhao, Microstructure of ultrahigh carbon martensite, Progress in Natural Science: Materials International. 28 (2018) 749–753. https://doi.org/10.1016/j.pnsc.2018.11.008.

[28] S. Liu, Q. Huang, L. Peng, Y. Li, C. Li, Microstructure and its influence on mechanical properties of CLAM steel, Fusion Engineering and Design. 87 (2012) 1628–1632. https://doi.org/10.1016/j.fusengdes.2012.06.008.

[29] L. Kučerová, I. Zetková, A. Jandová, M. Bystrianský, Microstructural characterisation and in-situ straining of additive-manufactured X3NiCoMoTi 18-9-5 maraging steel, Materials Science and Engineering: A. 750 (2019) 70–80. https://doi.org/10.1016/J.MSEA.2019.02.041.

[30] K. Kempen, E. Yasa, L. Thijs, J.P. Kruth, J. van Humbeeck, Microstructure and mechanical properties of Selective Laser Melted 18Ni-300 steel, Physics Procedia. 12 (2011) 255–263. https://doi.org/10.1016/J.PHPRO.2011.03.033.

[31] J. Feng, P. Zhang, Z. Jia, Z. Yu, C. Fang, H. Yan, H. Shi, Y. Tian, Microstructures and mechanical properties of

reduced activation ferritic/martensitic steel fabricated by laser melting deposition, Fusion Engineering and Design. 173 (2021) 112865. https://doi.org/10.1016/J.FUSENGDES.2021.112865.

[32] N. Allain-Bonasso, F. Wagner, S. Berbenni, D.P. Field, A study of the heterogeneity of plastic deformation in IF steel by EBSD, Materials Science and Engineering A. 548 (2012) 56–63. https://doi.org/10.1016/j.msea.2012.03.068.

[33] D.J. Child, G.D. West, R.C. Thomson, Assessment of surface hardening effects from shot peening on a Ni-based alloy using electron backscatter diffraction techniques, Acta Materialia. 59 (2011) 4825–4834. https://doi.org/10.1016/j.actamat.2011.04.025.

[34] Q. Huang, Development status of CLAM steel for fusion application, Journal of Nuclear Materials. 455 (2014) 649–654. https://doi.org/10.1016/j.jnucmat.2014.08.055.

[35] B. Zhang, L. Dembinski, C. Coddet, The study of the laser parameters and environment variables effect on mechanical properties of high compact parts elaborated by selective laser melting 316L powder, Materials Science and Engineering A. 584 (2013) 21–31. https://doi.org/10.1016/j.msea.2013.06.055.

[36] Y. Zhong, L. Liu, S. Wikman, D. Cui, Z. Shen, Intragranular cellular segregation network structure strengthening 316L stainless steel prepared by selective laser melting, Journal of Nuclear Materials. 470 (2016) 170–178. https://doi.org/10.1016/j.jnucmat.2015.12.034.

[37] D. Wang, C. Song, Y. Yang, Y. Bai, Investigation of crystal growth mechanism during selective laser melting and mechanical property characterization of 316L stainless steel parts, Materials and Design. 100 (2016) 291–299. https://doi.org/10.1016/j.matdes.2016.03.111.

[38] X. Wei, P. Zhang, Z. Yu, H. Yan, D. Wu, H. Shi, J. Chen, Q. Lu, Y. Tian, S. Ma, W. Lei, Effect of phase transformation on mechanical properties of Al16.80Co20.74Cr20.49Fe21.28Ni20.70 high entropy alloy coatings processed by laser cladding, Journal of Alloys and Compounds. 862 (2021) 158563. https://doi.org/10.1016/j.jallcom.2020.158563.

[39] Y. v. Milman, A.A. Golubenko, S.N. Dub, Indentation size effect in nanohardness, Acta Materialia. 59 (2011) 7480–7487. https://doi.org/10.1016/j.actamat.2011.08.027.